Journal of Nuclear Materials 558 (2022) 153358

Contents lists available at ScienceDirect

Journal of Nuclear Materials

journal homepage: www.elsevier.com/locate/jnucmat

Investigation of breakaway corrosion observed during oxide growth in pure and low alloying element content Zr exposed in water at 360°C

B. Ensor[a,b,*], A.T. Motta[a], A. Lucente[b], J.R. Seidensticker[c], J. Partezana[d], Z. Cai[e]

[a] The Ken and Mary Alice Lindquist Department of Nuclear Engineering, The Pennsylvania State University, 206 Hallowell Bldg, University Park, PA 16802 USA
[b] Naval Nuclear Laboratory, PO Box 1072, Schenectady, NY 12301 USA
[c] Naval Nuclear Laboratory, PO Box 79, West Mifflin, PA 15122 USA
[d] Westinghouse Electric Co., 1332 Beulah Rd. Pittsburgh, PA, 15235 USA
[e] Advanced Photon Source, Argonne National Laboratory, 9700 S. Cass Avenue, Argonne, IL 60439 USA

ARTICLE INFO

Article history:
Received 16 April 2021
Revised 24 August 2021
Accepted 18 October 2021
Available online 21 October 2021

Keywords:
Zirconium alloy
Breakaway
Corrosion
Synchrotron radiation

ABSTRACT

The addition of small concentrations of alloying elements to pure zirconium can prevent nuclear fuel cladding material from undergoing unstable oxide growth in aqueous environments at light water reactor operating temperatures. The role of alloying elements in stabilizing the oxide growth is examined in this paper, to better understand the oxide growth stabilization mechanism. To this end, a set of initial, short-duration corrosion experiments were performed, followed by oxide layer characterization. Specifically, ten model Zr alloys were selected to test the effect of small alloying additions on the alloy corrosion rate and corrosion breakaway. These alloys were corrosion tested in pure water in an autoclave at 360 °C for up to 70 days. The alloys included crystal bar Zr, sponge Zr, and model alloys with small concentrations of Sn, Fe, and Cr. After testing, the alloys were characterized using scanning electron microscopy (SEM) and synchrotron μ-X-ray fluorescence (μXRF) to study how the structure of the oxide and alloying element distribution related to unstable oxide growth. Initial results in the 360 °C water environment showed breakaway oxidation may be caused by unstable oxide growth due to heterogeneous distribution of the alloying elements. Heterogeneous distribution of alloying elements was correlated to the occurrence of unstable oxide growth (either nodule-like, grain boundary penetration, or differential grain-to-grain growth). It is possible that this heterogeneity, made possible by low alloying element content, can cause breakaway corrosion, but further study is warranted.

1. Introduction

Early testing of zirconium alloys performed in the 1950′s and 60′s demonstrated that unalloyed zirconium metal, whether made from crystal bar or sponge[1], exhibits variable and unstable oxidation behavior. In particular, when the material is exposed to high temperature water or steam, breakaway[2] corrosion is often observed, whereby the growing oxide starts to flake and spall during corrosion [1,2,3]. Furthermore, the corrosion resistance of pure Zr varies from ingot to ingot, such that the material was deemed not to be suitable for use as nuclear fuel cladding. Fortunately, it was found that the addition of relatively small amounts of alloying elements made zirconium alloys significantly more resistant to corrosion than the pure material, causing the corrosion rate to decrease and made oxide growth more stable and reproducible [1]. However, since the main impetus in the past decades has been to optimize alloy composition and thermomechanical treatment so that better performance and stable oxide growth could be achieved rather than investigating the fundamental principles by which alloying elements stabilize growth, the fundamental mechanism for the stabilization of corrosion provided by low levels of alloying elements is still not understood today [1]. Moreover, when zirconium alloys are used beyond their normal conditions (e.g., high temperature accident scenarios) unstable oxide growth can occur. Thus, it is of great interest to understand the cause of these instabilities, as this could allow the design of better performing alloys. In this paper, the causes of breakaway corrosion in unalloyed Zr are studied

* Corresponding author at: PO Box 1072, Mail Stop 102, Schenectady, NY 12301, USA.
E-mail address: brendan.ensor@unnpp.gov (B. Ensor).

[1] Crystal bar Zr is produced via the Van Arkel process which yields highly pure Zr, while sponge Zr is produced from a direct separation process (the Kroll process) [4].

[2] The historic term 'breakaway' corrosion is used throughout this paper to refer to a subset of unstable oxide growth observed in pure Zr and Zr alloys with low alloying element content, as defined in the next section.

https://doi.org/10.1016/j.jnucmat.2021.153358
0022-3115/

to better understand the role of alloying elements in the stabilization process. Zr alloy samples exhibiting unstable oxide growth are characterized in a set of initial experiments to understand the differences in the corrosion process when compared to stable oxide growth and the results discussed in light of existing knowledge.

2. Background

In alloys which exhibit stable oxide growth when exposed to high temperature water environments, such as Zircaloy-4, a protective oxide layer develops which slows down further oxidation of the metal [4,5,6,7]. In many of these alloys, at a critical point during oxide growth, a kinetic transition takes place, at which point the oxide layer loses its protective character, allowing easy access of water to the metal-oxide interface, which results in an increase of the corrosion rate. This change in oxide growth kinetics is known as the *oxide transition*. Prior to this change the oxide is said to be in the pre-transition regime. After transition, the corrosion rate returns to the corrosion kinetics of the bare metal and the newly-formed oxide again becomes protective, slowing the oxidation until it reaches a new transition, in a cyclic process. In contrast, when the oxide loses its protective character and oxide growth becomes unstable (e.g., non-planar oxide growth), the alloy is said to experience 'breakaway' corrosion.

The departure from stable growth normally entails inhomogeneous oxide growth, exhibiting preferential advance along specific microstructure features of the bare metal, such as different grains, grain boundaries, and second phase particles [8]. This non-homogeneous growth can lead to the development of compatibility stresses which may mechanically fracture the oxide layer. As the oxide loses its protective character, its color turns from dark gray or black to white and the oxide layer may start to flake off. Thus, breakaway corrosion exhibits unstable oxide growth. Unstable oxide growth can be defined as having any of the following characteristics:

- Whitish, spalling oxide layer
- Significant and sustained acceleration of the corrosion rate[3]
- Significant deviation from planar oxide growth into the metal
- Formation of nodules or other local regions of advanced oxide growth

Breakaway oxidation is one mode of unstable oxide growth and was observed in pure Zr during early alloy development. Reference [8] shows SEM micrographs illustrating the marked contrast between oxide growth during stable corrosion (Zircaloy-4) and unstable corrosion (pure Zr). A note on terminology is important when discussing this phenomenon. The similarities between breakaway corrosion and the oxide transition in Zr alloys have been noted by various researchers [3,7,9]. In fact, the words 'transition' and 'breakaway' were used interchangeably in early research [2,3,7,9,10,11]. Further, the term 'breakaway' is occasionally used to refer to higher corrosion kinetics under loss-of-coolant accident (LOCA) conditions, exposures to steam and nitrogen mixes at higher temperatures, or long-term in-reactor acceleration of Zr alloy corrosion rates [12]. For the purposes of this study, the term 'breakaway' describes corrosion of pure Zr and Zr alloys with low alloying element content (defined here and throughout this paper as >99.5 wt.% Zr) at typical reactor temperatures. This breakaway corrosion is characterized by the formation of white oxide and highly accelerated oxide growth wherein non-planar oxide grows rapidly into the metal.

As was evident during early alloy development, small amounts of alloying elements can be influential on corrosion performance [1]. Although research has been performed on the spatial distribution of the alloying elements, detailed knowledge is lacking in part because the alloying amount in solid solution in the alloys is typically below the detection limits of standard methods, such as energy-dispersive X-ray spectroscopy (EDS). The recent development of advanced techniques (e.g., atom probe tomography and secondary-ion mass spectrometry) has led to renewed interest in studying the distribution of alloying elements in Zr alloys [13,14,15,16].

It was observed during corrosion tests on pure Zr in 500 °C steam and 350 °C oxygen that locally thicker oxide layers were formed, which were referred to as 'pustules[4]' or 'bumps' [17,18]. Similarly the formation of 'nodules' has been observed during LOCA experiments and been associated with breakaway corrosion under these conditions [19,20] Additionally, nodular corrosion has been observed on some Zr alloys during corrosion in boiling water reactors [4]. These are examples of the morphology of local unstable oxide growth on pure Zr which this paper investigates.

A few theories have been proposed to explain a rapid acceleration of corrosion of pure Zr in water or loss of protectiveness of oxide layers in zirconium alloys at elevated temperatures (>400 °C), including the development of interconnected porosity (which is similarly used to explain transition), cracking of the oxide due to inhomogeneous growth, and the presence of hydrogen [2,10,11,18,19,20,21]. Since it is common for mostly pure Zr or Zr alloys with low alloying element content to undergo breakaway corrosion during standardized corrosion tests (e.g., at 360 °C in water or 400 °C in steam) [1,8], it is natural to study the influence of low alloying element contents on breakaway susceptibility. Consequently, the distribution of alloying elements and their role on the stabilization of oxide growth is the main focus of this study.

3. Experimental technique and materials

3.1. Materials

Ten model Zr alloys were produced by arc melting with a range of alloy compositions, generally on the low alloying element content range. These samples were chosen to represent a range of alloys with key constituent elements in low concentrations to determine how the presence of these different elements can affect the onset of breakaway corrosion.

The alloys were prepared by Thermacore, Inc. by arc-melting in a pure argon environment. Each arc-melted button weighed approximately 300 gs and was melted three times to ensure homogeneity. The arc-melted buttons were β-solution treated at 1050 °C for 30 min in a vacuum furnace, hot-rolled after pre-heating between 580 - 720 °C[5] for 10 min in vacuum and cold-rolled three times (55–58% total reduction) to a final thickness. Between each rolling step, the cold-rolled sheets were intermediate-annealed in vacuum at a temperature between 580 and 720 °C for 30 min depending on the alloy system[5]. A final anneal in vacuum (800 °C for 30 min) was performed, which for the sponge Zr could have been in the very low $\alpha+\beta$ region (when considering the effects of oxygen), and for Zr-0.2Fe and the Zr-Fe-Cr ternary alloys (with very low oxygen content) was in the $\alpha+\beta$ region. For the crystal bar Zr, Zr-0.1Cr, and the Zr-Sn binary alloys this final anneal was

[3] The cyclical corrosion process can be fit as approximately linear after long exposure times [33]. While many factors can accelerate corrosion, and it is common to see a slow acceleration in corrosion rates in subsequent cycles, unstable oxide growth is defined as being a significant (at least a 50%) increase from this process.

[4] 'Pustules', 'bumps', and 'nodules' in the early literature were all descriptions of similar phenomena of locally thicker oxide layers over the surface of the material and are not significantly different from one another.

[5] 580 °C for ZC1, ZS1, SN1, SN2, and SN3, 650 °C for CR1,and 720 °C for FC1, FC2, FC3, and FE1.

Table 1
List of model alloys and chemical analysis of material; key elements for the model alloys, color coded by alloy system, are bolded. The phase of the final anneal 800 °C for 30 min) of the material is provided ($\alpha \rightarrow \alpha+\beta$ transition estimated in parentheses).

Chemical Analysis #1 (Luvak Inc.), Weight%									
Sample	Nominal Composition	H	C	N	O	Fe	Cr	Hf	Anneal
Crystal Bar	Zr (crystal bar)	0.0014	0.007	<0.005	0.011	0.0061	<0.005	0.035	–
Sponge	Zr (sponge)	0.0050	0.004	<0.005	0.058	0.0200	0.013	0.028	–
Chemical Analysis #2 (RJ Lee Group), Weight%									
Sample	Nominal Composition	H	C	N	O	Fe	Cr	Sn	Anneal
ZC1	Zr (crystal bar)	0.0017	0.011	0.002	0.019	0.006	<0.002	0.002	α (~850 °C)
ZS1	Zr (sponge)	0.0019	0.012	0.003	0.100	0.026	0.005	<0.002	Low $\alpha+\beta$ (~750 °C)
FC1	Zr-0.1Fe-0.05Cr	0.0012	0.007	0.002	0.015	0.100	0.058	<0.002	Low $\alpha+\beta$ (~750 °C)
FC2	Zr-0.05Fe-0.025Cr	0.0012	0.008	0.001	0.015	0.056	0.024	0.002	Low $\alpha+\beta$ (~750 °C)
FC3	Zr-0.05Fe-0.05Cr	0.0013	0.005	0.001	0.007	0.050	0.055	<0.002	Low $\alpha+\beta$ (~750 °C)
CR1	Zr-0.1Cr	0.0017	0.006	0.002	0.018	0.006	0.088	<0.002	α (~850 °C)
FE1	Zr-0.2Fe	0.0015	0.010	0.003	0.010	0.180	0.003	<0.002	Low $\alpha+\beta$ (~750 °C)
SN1	Zr-0.2Sn	0.0016	0.006	0.001	0.010	0.004	<0.002	0.180	α (~865 °C)
SN2	Zr-0.4Sn	0.0014	0.008	0.001	0.010	0.007	<0.002	0.370	α (~865 °C)
SN3	Zr-0.1Sn	0.0012	0.005	0.001	0.020	0.003	<0.002	0.110	α (~865 °C)

in the α region [22,23,24]. The heat treatment resulted in the formation of an equiaxed microstructure with grain size on the order of ~10 μm. Following this, standard surface treatment (pickling) was done in a solution of $45H_2O$:$45HNO_3$:10HF. After the heat treatment and rolling, the sheets were cut into ~2.5 cm x 2.5 cm coupons, with a thickness of ~0.75 mm. The coupons were marked with a metallographic stamper for reference.

Sponge and crystal bar samples were tested by Luvak Inc. using hot vacuum extraction for hydrogen content determination, combustion infrared detection to determine carbon content, inert gas fusion to determine oxygen and nitrogen content, and direct current plasma emission spectroscopy to determine the transition metal content of the 10 alloys. A piece of each prepared coupon was sent for chemical analysis to the RJ Lee Group where LECO analysis was used to determine C, N, and O content, hot vacuum extraction was used to determine H, and Inductively Coupled Plasma (ICP) was used to determine Cr, Fe, and Sn contents. The results of these elemental analyses and a list of the model alloys are shown in Table 1.

The low alloying element content in crystal bar Zr should be noted (0.0061 wt% Fe and <0.002 wt% Cr). These values are below the theoretical solubility limits of these elements in Zr, and therefore no precipitates are expected to be formed. This stock of pure crystal bar Zr was used to create the remaining model alloys, and as can be seen, with the exception of purposeful alloy additions, the elemental concentrations are consistent with the elemental concentrations in the starting materials. The crystal bar Zr and the Zr-Sn binary alloys had no precipitates, while the Fe and Cr concentration in the remaining alloys had sufficient alloying element content to produce precipitates. This included the sponge Zr which had 0.02 wt% Fe and 0.013 wt% Cr and thus is expected to show some precipitates, which were in fact observed using SEM. The only other major difference between crystal bar and sponge Zr was an order of magnitude higher O content (from ~0.01 wt% in the model alloys made from crystal bar Zr to ~0.1 wt% in sponge Zr). Sponge Zr exhibited larger differences between separate chemical analyses of individual samples than did crystal bar Zr, indicative of the inherent variability in the starting material.

Since the addition of alloying elements reduces the tendency for breakaway oxidation, removing them altogether should promote unstable oxide growth. Furthermore, by varying the amounts of each of these elements, the minimum amounts necessary for protective behavior could be studied.

3.2. Corrosion testing and characterization

Two samples of each model alloy were tested in an autoclave at 360 °C at Westinghouse. Four control samples of Zircaloy-4 were corroded alongside the model alloys. The corrosion tests were performed in a degassed autoclave with static pure water of neutral pH following ASTM G2 [25]. For these initial experiments, samples were corroded for a maximum of 70 days, with some coupons removed earlier for examination (particularly if signs of breakaway corrosion were apparent) since previous experiments have shown that only short exposures are needed to cause breakaway corrosion [1,8].

After the corrosion tests, the oxide layers formed on these samples were characterized using a number of techniques to investigate the underlying causes of breakaway corrosion. Samples were first imaged using SEM. This was accomplished both by preparing cross-sectional samples (as described in [26]) and by using the Focused Ion Beam (FIB), an FEI Helios NanoLab 660, to mill into the oxide while imaging the sample. Milling was performed using 30 keV gallium ions at a current of 9.3 nA. After milling, the surface was cleaned for imaging using a 0.79 nA current. Prior to milling either Pt or C were electron beam deposited on the surface to prevent surface damage. The FEI Helios NanoLab 660 was also used to perform Electron Back Scatter Diffraction (EBSD) to determine grain orientation on some samples (which were also examined using an additional SEM, a Zeiss SIGMA VP-FESEM) [27]. The FEI software Aztec was used for EBSD analysis using the Kikuchi bands to index the crystal structures investigated and to determine grain orientation.

Two samples were examined using microbeam synchrotron radiation fluorescence to examine the distribution of alloying elements in relation to the oxide morphology prior to and after breakaway corrosion. This was performed at the 2-ID-D beamline at the Advanced Photon Source (APS) at Argonne National Laboratory. The goal was to obtain high-resolution X-ray fluorescence (XRF) data maps of the oxide and the metal to determine the alloying element distribution ahead of the oxide front, as has been done previously [26,28,29]. An optical microscope at the beamline was used to correlate the XRF data to the oxide morphology.

The X-ray beam energy used was 8.34 keV and the spot size was 0.2 μm x 0.2 μm. For the experiment, a cross sectional sample was attached onto an aluminum stud which was tilted into the beam's path, causing it to hit the sample at an incident angle of 14° creating a footprint of 0.2 μm x 1 μm on the sample (larger

size parallel to the metal-oxide interface). The mean free path of the incoming X-ray (8.34 keV) is ~12 μm and the resulting L or K edge X-rays produced for the elements of interest would be even less, thus the technique is particularly sensitive to the surface region. A Ge (Li) Canberra solid state detector was used to acquire fluorescence data at each point. Prior to acquiring high-resolution maps, a quick fluorescence map with large step size was acquired on each sample to identify the regions to examine in greater detail. For the high-resolution maps, a step size of 1 μm and dwell time of 1.5 s was used on the crystal bar Zr sample and a step size of 0.25 μm and dwell time of 6 s was used on the sponge Zr sample. After each map, individual locations were selected for long dwell time acquisitions (60 s for crystal bar and 100 s for sponge). In all cases studied, the fluorescence counts from the rough maps and high-resolution maps scaled and were repeatable. The counts in the ~0.3 keV energy range near the fluorescence spectral lines of interest (Zr L, Cr K_α, Fe K_α, and Sn L) were then collected and recorded.

To account for variability in signal incident on the sample and reaching the detector, the fluorescence counts were normalized to the incident X-ray beam. Following this operation, the alloying elements counts were normalized to the Zr L counts. Error in the fluorescence measurement is reported as the standard deviation of the counts but does not account for all forms of possible measurement error and uncertainty. Note that the elemental measurements reported here are obtained by defining regions of interest in the fluorescence spectra, which contain the relevant fluorescence peaks for each element. In particular no background subtraction was performed as the full fluorescence spectra were not recorded for these initial investigations. Recording and using the full spectra are recommended for future experiments to more quantitatively determine the distribution of low levels of alloying element content. Nevertheless, this simple technique, although not quantitative, provides a reliable estimate of the variation in element concentration in different locations. Fluorescence analysis has been used in the past to determine alloying element concentration and can detect variations on the order of one ppm [28].

4. Results and discussion

4.1. Analysis of Zr and model Zr alloys corroded in autoclave with 360 °C water

Previous research has shown that pure Zr alloys, both crystal bar and sponge, sooner or later undergo breakaway corrosion when exposed to a 360 °C autoclave environment [8]. Fig. 1 shows weight gain data for the model alloy samples tested in this study; two coupons of each sample were tested, as shown.

The coupons were tested for up to 70 days. One sample of crystal bar Zr and one of the samples of Zr-0.2Sn underwent breakaway corrosion in 10 and 3 days, respectively, exhibiting white spalling oxide. Additionally, ZS1 (sponge Zr) exhibited some areas of white oxide on the coupon surface. This observation of white spots, along with weight loss was used as an initial criterion for breakaway corrosion, as shown in Fig. 2.

Surprisingly, among alloys with elemental additions, only the Zr-0.2Sn sample showed signs of breakaway corrosion, in this case after only a 3-day exposure. This suggests that small amounts of alloying element content (as little as Zr-0.05Fe-0.025Cr) could stabilize oxide growth. Samples that did not show breakaway exhibited mostly black, protective oxide, characteristic of stable oxide growth. This included a Zr-0.1Sn sample that was exposed for 70 days without showing breakaway oxidation. As previously mentioned, the occurrence of breakaway corrosion cannot always be precisely predicted: some samples experience breakaway quickly, while others do not experience breakaway corrosion for some time [1,8]. It is also possible that there is a threshold in the amount of Sn needed in a particular grain to cause local accelerated corrosion in a grain; for instance, as can be seen in Fig. 1, the Zr-0.4Sn alloy shows ~40–50% higher weight gain than the Zr-0.1Sn. Given the

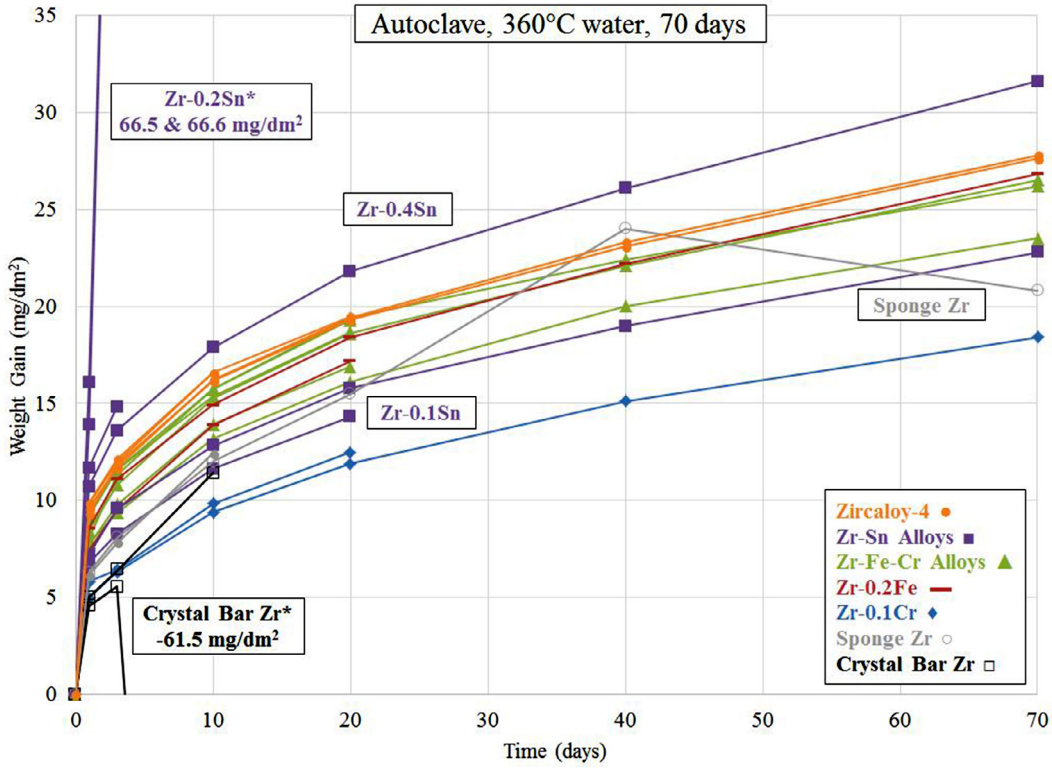

Fig. 1. Weight gain data for model Zr alloys corroded in autoclave for 70 days with 360 °C water. *Samples noted with an asterisk underwent breakaway oxidation.

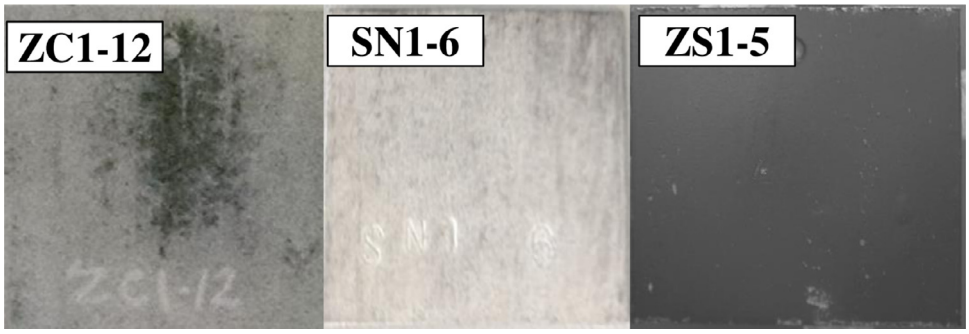

Fig. 2. Images of three corrosion coupons following exposure in a 360 °C autoclave. ZC1–12 (crystal bar - 10 days), SN1–6 (Zr-0.2Sn - 3 days), and ZS1–5 (sponge - 70 days) exhibit varying degrees of white spalling oxide, characteristic of breakaway oxidation.

results of the Zr-Sn alloys (Zr-0.1Sn – lowest weight gain, no breakaway; Zr-0.2Sn – breakaway; Zr-0.4Sn – 40–50% higher weight gain than Zr-0.1Sn, no breakaway), it is postulated that the Zr-0.1Sn alloy may not have sufficient Sn to exceed this threshold in most grains, while the Zr-0.4Sn alloy does. Following this theory, the Zr-0.2Sn may have a mixture such that some grains exceed the threshold, while others do not, leading to potential differential oxide growth from grain to grain, which may lead to a breakaway corrosion condition.

With the exception of the samples that underwent breakaway corrosion, none of the alloys tested in the autoclave went beyond the oxide transition. However, the alloys did show a wide variability in pre-transition kinetics. Final weight gain values measured after 70 days ranged from 18.4 mg/dm^2 in Zr-0.1Cr to 31.6 mg/dm^2 in Zr-0.4Sn, equivalent to 1.2 μm to 2.2 μm of oxide. Zircaloy-4 coupons showed an average weight gain of 27.7 mg/dm^2 (corresponding to 1.9 μm). The individual kinetics for each alloy are given by Eq. (1),

$$w = A \times t^n \quad (1)$$

where w is the weight gain of the alloy, t is exposure time, and A and n are constants. The calculated values of the exponent n all fell within a tight range in the sub-cubic region from 0.24 to 0.3. The corrosion kinetics observed in this study (n=~0.2–0.3 for Fe-Cr-Sn alloys) are in agreement with previous determinations of pre-transition corrosion kinetics of model Zr alloys (including both Zr-Sn and Zr-Fe-Cr alloys) [8].

4.2. Characterization of model Zr alloys corroded in autoclave using SEM

After autoclave corrosion testing, the oxide layers formed on the model alloys were examined using SEM (prepared both in cross-section and using the FIB). Fig. 3 shows six SEM cross-section images showing stable oxide growth. In the samples that did not experience breakaway corrosion, mostly stable oxide growth is observed, although regions of preferential growth may be evident along different metal grains or grain boundaries (e.g., along a grain boundary in Fig. 3(a) and in different grains in Fig. 3(c)). Fig. 3(d) shows a region of stable oxide growth in the sponge Zr sample, which in other locations exhibited unstable oxide growth. The oxides in the stable regions of the model alloys were similar in appearance to Zircaloy-4, which is shown in Fig. 3(f).

In contrast, samples in which breakaway corrosion has occurred show a much less uniform metal-oxide interface. Fig. 4 shows typical SEM micrographs of breakaway oxides formed on crystal bar Zr (top) and on Zr-0.2Sn (bottom) after exposure for 10 and 3 days, respectively.

During breakaway corrosion, 'finger'-like oxide growth along grain boundaries is often observed, as shown in Fig. 4(b) and (d) and evidenced by the approximate 10 μm spacing in a number of the fingers. The dendritic features also grow in regions where there are no grain boundaries, such as in Fig. 4(c), as it is unlikely that all the 'fingers' in Fig. 4 are along grain boundaries, as the metal grain size is on the order of 10 μm. SEM micrographs during FIB milling are shown in Fig. 4 (a and c), while those acquired after preparation in cross-section are shown on the right (b and d). The morphologies of these breakaway oxide layers are similar to those seen in previous studies [8]. This morphology of oxide growth is a consequence of breakaway oxidation and the penetrating oxide 'fingers' are formed along the easiest paths for rapid corrosion in each case.

When breakaway corrosion occurs, in addition to the surface of the samples turning white, it was clear that the surfaces were no longer smooth on a microscopic level. As a result, plan-view examinations of these oxide layers were undertaken to characterize these inhomogeneities. Fig. 5 shows plan-view SEM micrographs taken of oxide layers formed on crystal bar Zr and Zircaloy-4 showing widespread spalling of the oxide in crystal bar Zr, which underwent breakaway corrosion, compared to Zircaloy-4, which exhibits stable oxide growth. The surface of the crystal bar Zr on the left in Fig. 5 appears rough, and shows oxide spalling, while the right SEM micrograph taken from Zircaloy-4 is smooth, and shows no oxide spalling.

An interesting observation in the examination of plan-view samples was that after testing the model Zr alloys exhibited inhomogeneities on their outer surfaces. Fig. 6 shows SEM micrographs of nodule-like formations on the outer surface of four model Zr alloy samples corroded for up to 70 days.

Small nodule-like oxide formations can be seen on the surface of the model Zr alloys in Fig. 6(a) – (c), and (e) – (f). In the sponge Zr sample, ZS1–5, which was corroded for 70 days and is shown in Fig. 6(d), the nodule appears much larger. This sample showed signs of beginning to break away (white spots of oxide visually apparent) and these larger areas of spalling oxide resemble the surface of samples that have undergone breakaway corrosion. This suggests that such inhomogeneities could be precursors of breakaway.

The initial diameter of the nodule-like formations is ~5 μm. These nodules were seen on the surface of every model alloy sample as soon as 3 days after exposure to the corrosion environment. This includes some of the alloys in Fig. 6 which had a final treatment in the low $\alpha+\beta$ region (thus potentially creating β-Zr and segregating the alloying elements) and which could be the cause of the nodules for these alloys. However, the final recrystallization anneals for the crystal bar Zr, Zr-0.1Cr, and Zr-Sn binary alloys were in the α region and these alloys also exhibited nodules on the surface. Interestingly, the nodule-like formations were also associated with regions of advanced oxide growth. Fig. 7 shows SEM micrographs of a cross-section of the oxide layer underneath the nodule-

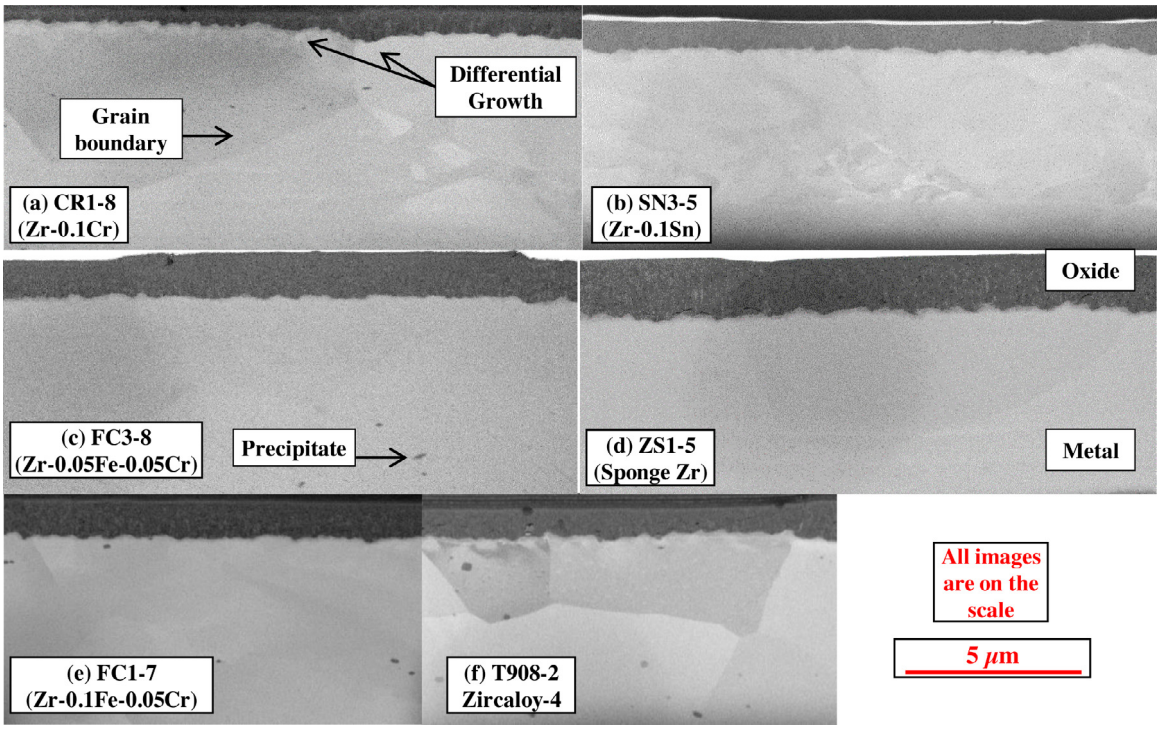

Fig. 3. SEM images of six model Zr alloys corroded in autoclave with 360 °C water for 20 (a, b, c, e & f) and 70 days (d) exhibiting stable oxide growth in the regions examined: (a) CR1–8 (Zr-0.1Cr), (b) SN3–5 (Zr-0.1Sn), (c) FC3–8 (Zr-0.05Fe-0.05Cr), (d) ZS1–5 (sponge Zr), (e) FC1–7 (Zr-0.1Fe-0.05Cr), (f) T908–2 (Zircaloy-4). All images are on the same scale.

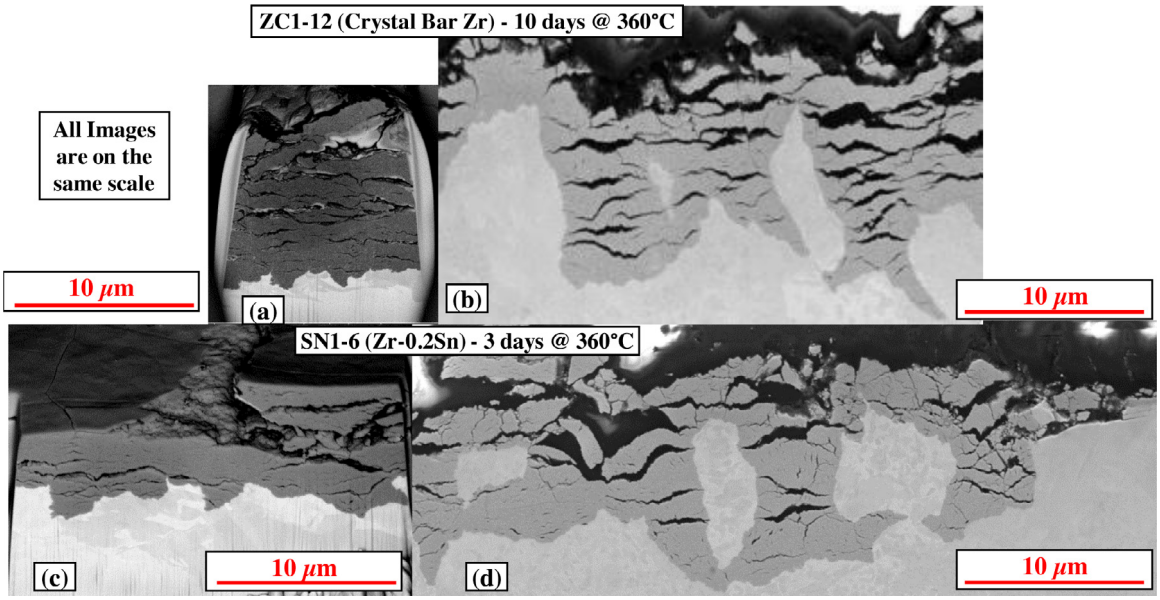

Fig. 4. SEM images of breakaway oxidation in model Zr alloys corroded in autoclave with 360 °C water for 3 days (SN1) and 10 days (ZC1): (a) ZC1–12 (Crystal bar Zr) FIB prepared SEM micrograph, (b) ZC1–12 (Crystal bar Zr) cross-section and polish prepared SEM micrograph, (c) SN1–6 (Zr-0.2Sn) FIB prepared SEM micrograph, and (d) SN1–6 (Zr-0.2Sn) cross-section and polish prepared SEM micrograph.

like regions. The regions directly underneath the nodules showed thicker oxide layers. The oxide layer shown on Fig. 7(a) exhibits significant growth instability, advancing much further into one region than into the neighboring regions. This differential growth is normally associated with cracking and spalling of the oxide layer, and this is evident in all Fig. 7 images. In Fig. 7(b) a similar unstable oxide layer advancement is observed. Note that the globe of oxide which appears separated from the rest of the oxide comes from the three-dimensional nature of the unstable growth. In both Fig. 7(a) and Fig. 7(b), the regions of advanced oxide growth occurred on what appeared to be single metal grains. However, the localized advancement of the oxide in Fig. 7(c) could be related to preferential oxide growth along a grain boundary, also leading to oxide cracking. Finally, advanced oxide growth in sponge Zr and

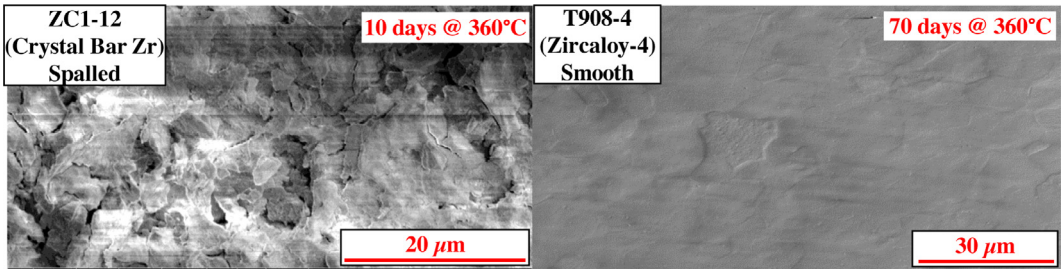

Fig. 5. SEM images of the surface of two zirconium alloy samples corroded in 360 °C water in autoclave; the sample on the left underwent breakaway corrosion after 10 days and shows a rough, spalling surface, the sample on the right shows a smooth surface characteristic of stable growth after 70 days of exposure.

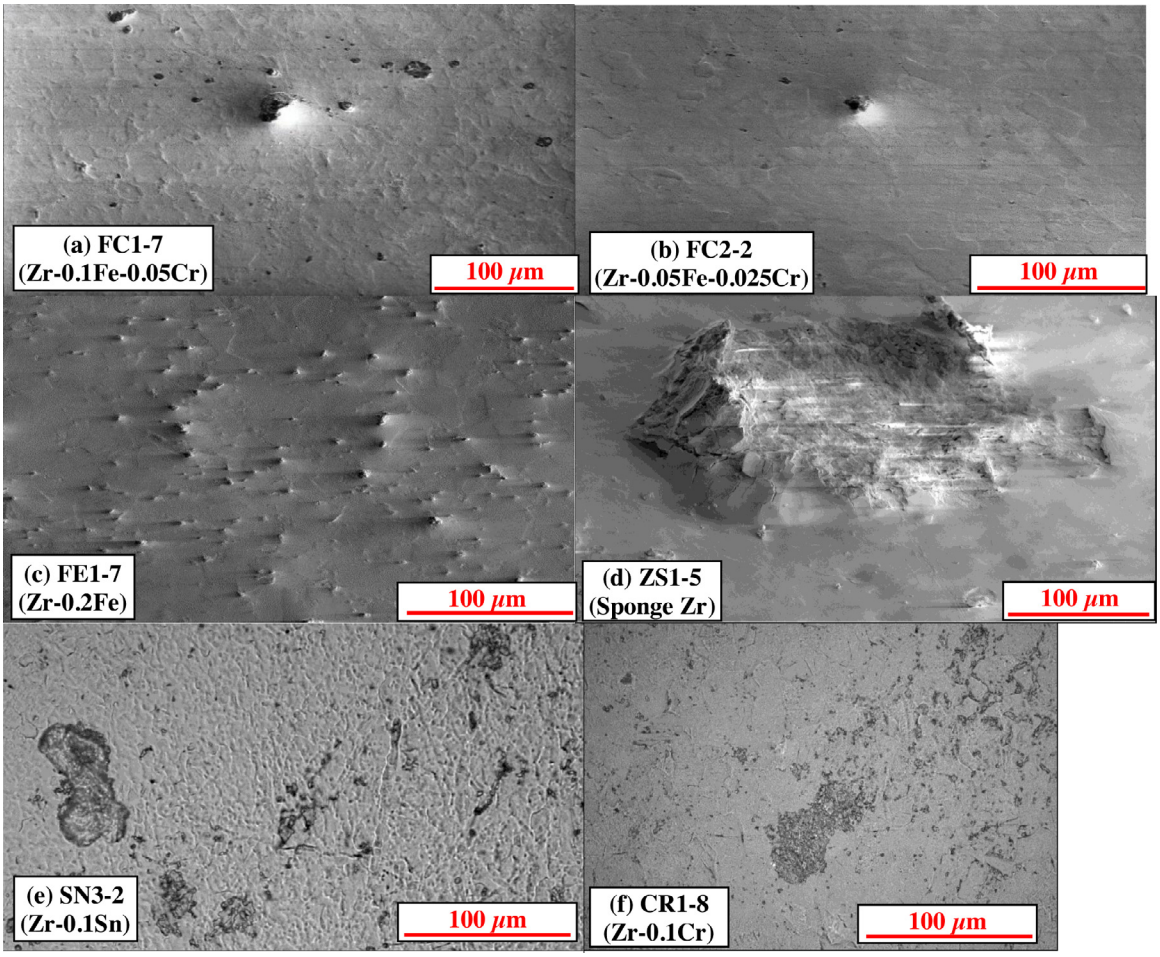

Fig. 6. Optical and SEM images of the surface of six model Zr alloys corroded in autoclave with 360ºC water for 20 (a, c, & f) and 70 days (b, d, & e): (a) FC1–7 (Zr-0.1Fe-0.05Cr, (b) FC2–2 (Zr-0.05Fe-0.025Cr), and (c) FE1–7 (Zr-0.2Fe) showing small surface nodules, (d) ZS1–5 (sponge Zr) showing the formation of a large surface nodule, and (e) SN3–2 (Zr-0.1Sn) and (f) CR1–8 (Zr-0.1Cr) showing small surface nodules.

crystal bar Zr is observed in Fig. 7(d) and (e) from the nodule-like formation. In these cases, the nodule like formation is accompanied by extensive oxide cracking.

The regions of advanced oxide growth shown in Fig. 7 are not seen in zirconium alloys which show stable oxide growth during testing in 360 °C water, such as Zircaloy-4, (which also showed no small nodules). Since the alloying content of the alloys tested and shown in Fig. 6 is much lower than that in commercial Zr alloys, the absence of these alloying elements in particular regions could be correlated to the occurrence of unstable growth (since even in 'pure' Zr there is some concentration of alloying elements present).

Thus, one possible cause for differential oxide growth is a heterogeneous distribution of the alloying elements in the alloy. This heterogeneous distribution could cause corrosion to vary locally, because of the potential effect of the alloying elements on the oxide conductivity and space charge formation in the oxide layer [30]. Alternatively, as described above, it is possible that for the Zr-Sn binary system there is a threshold for the amount of Sn in metal grains above which accelerated corrosion occurs. If the amount of Sn in the alloy is near this threshold, then grain-to-grain differential growth could lead to large stress buildup and a breakaway corrosion condition. To investigate the possible influence of alloying elements on onset of breakaway, the distribu-

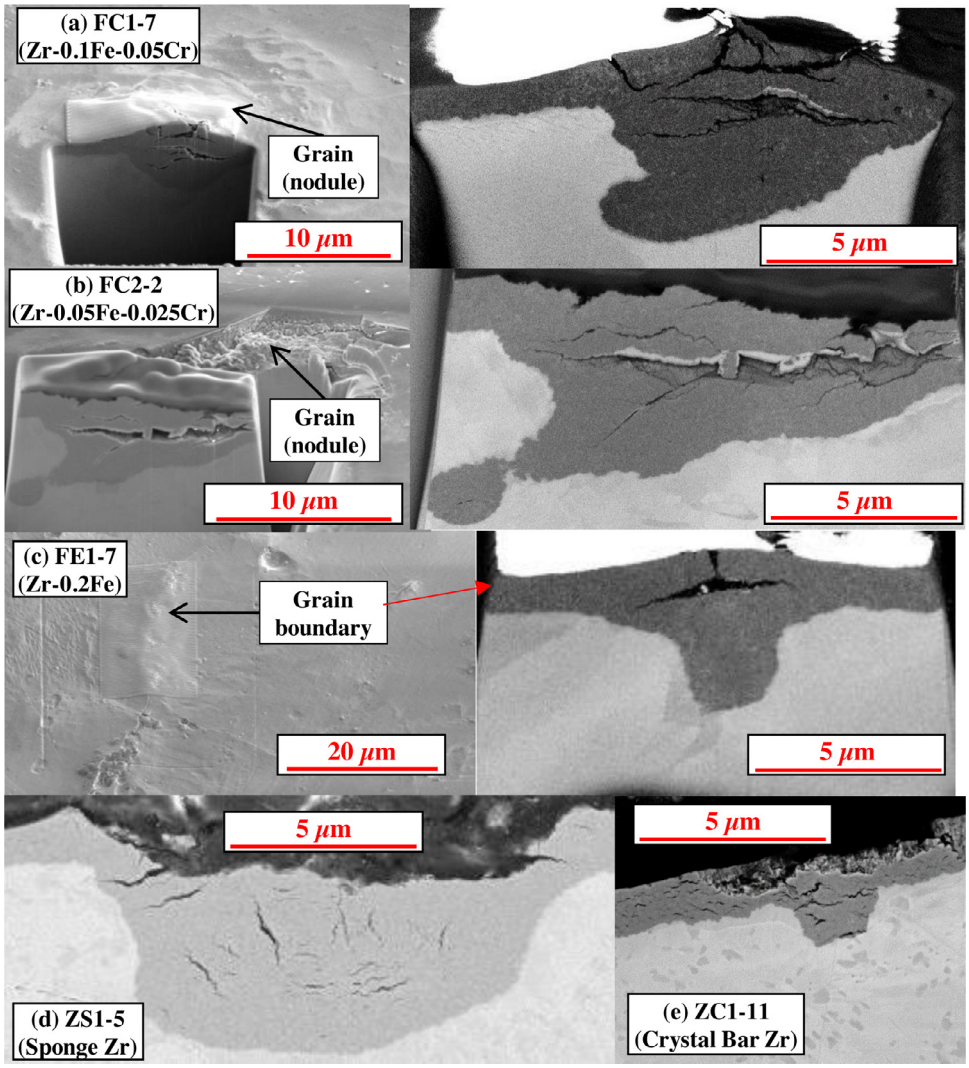

Fig. 7. Advanced oxide growth beneath nodule-like formations on five model Zr alloys corroded in autoclave with 360 °C water for 10 (e), 20 (a & c), and 70 days (b & d). (a)-(c) acquired after selectively milling using the FIB, (d)-(e) acquired from sample created in cross-section and polished.

tion of the alloying elements ahead of the oxide front needs to be studied. A preliminary such study is shown in the following section.

4.3. Synchrotron X-ray fluorescence mapping on samples with unstable oxide growth

Characterization of the oxide layers formed on model Zr alloys showed that the oxide layer often grew unevenly into the metal. An effort was made to determine the distribution of the alloying elements in the samples at specific locations ahead of the moving front. To this end, samples were studied at the APS using microbeam synchrotron X-ray fluorescence (XRF). Because for an X-ray energy of 8.34 keV the elemental sensitivity to Fe and Cr is quite high, this examination permits the study of the alloying element variability ahead of the oxide front even at very low alloying element levels.

The first sample examined was one of crystal bar Zr, which had undergone breakaway corrosion after exposure for 10 days. During corrosion this sample developed a 'finger'-like penetrating oxide morphology, as shown in Fig. 4 (a-b). XRF maps were acquired to obtain a measure of the alloying element content in the metal both in front of and to the side of some of these oxide fingers. Fig. 8 shows an optical microscope image of the metal-oxide interface acquired from the area where the fluorescence map was acquired. The oxide fingers are visible in Fig. 8 as black protrusions penetrating into the Zr metal in gray. The region ahead of the oxide, which shows slightly different contrast is thought to be rich in oxygen, as was seen previously [15]. Specific locations were selected in the metal for examination using XRF with long dwell times (60 s) so that good counting statistics could be obtained. This was done both in areas where the oxide fingers were not penetrating (A, D, and E) and where oxide fingers were penetrating (C and B), as shown in Fig. 8. The raw fluorescence results (normalized to the incident X-ray flux and to the Zr L counts) from this examination are shown in Fig. 8, in counts for a given energy region of interest (ROI). Although the arbitrary ROI range selection does not allow for quantitative determination of alloying element concentrations, the results from one location can be qualitatively compared with the others as long as the ROIs remain constant throughout the experiment. Note that the differences in the values reported only indicate that more or less alloying elements are present and do not indicate how much more or how much less is in each location (e.g., there is not necessarily twice the amount of Fe in location E compared to location A in Fig. 8). However, the magnitude of the differences (at least ~2x for each element on average), was considered meaningful to indicate differences in content from location to location.

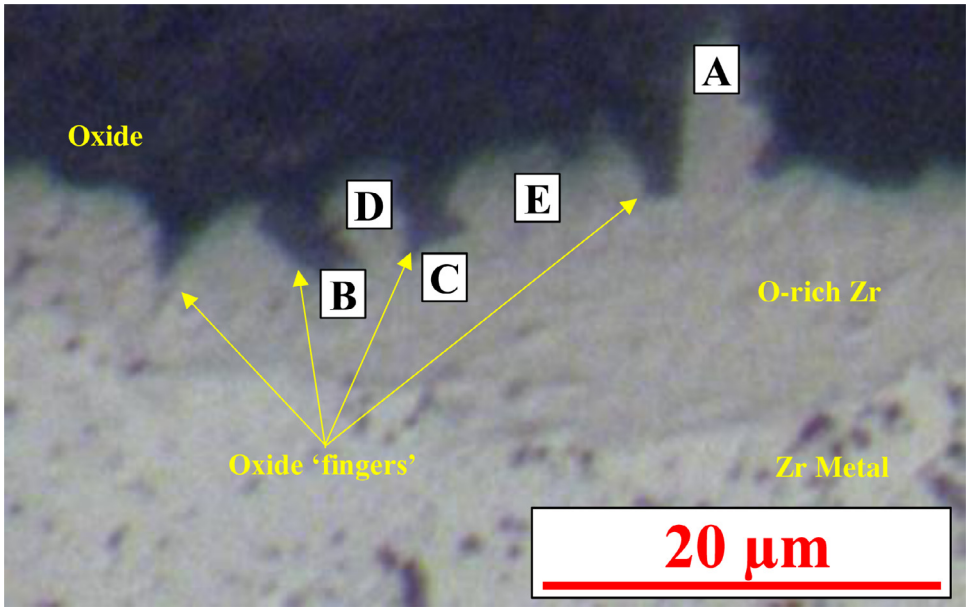

Fig. 8. (Top) Optical image of crystal bar Zr examined at the APS 2-ID-D beamline after a 10-day exposure at 360 °C. The black is the oxide and the gray is the metal. (Bottom) Synchrotron XRF data acquired at five locations for 60 s using the APS 2-ID-D beamline; for a given site, the Sn L, Cr K_α, and Fe K_α fluorescence counts are given normalized to the Zr L along with a description of the location; as can be seen, locations where the oxide did not penetrate have higher alloying element contents. Error based on standard deviation of the fluorescence counts before normalization and does not account for all forms of uncertainty.

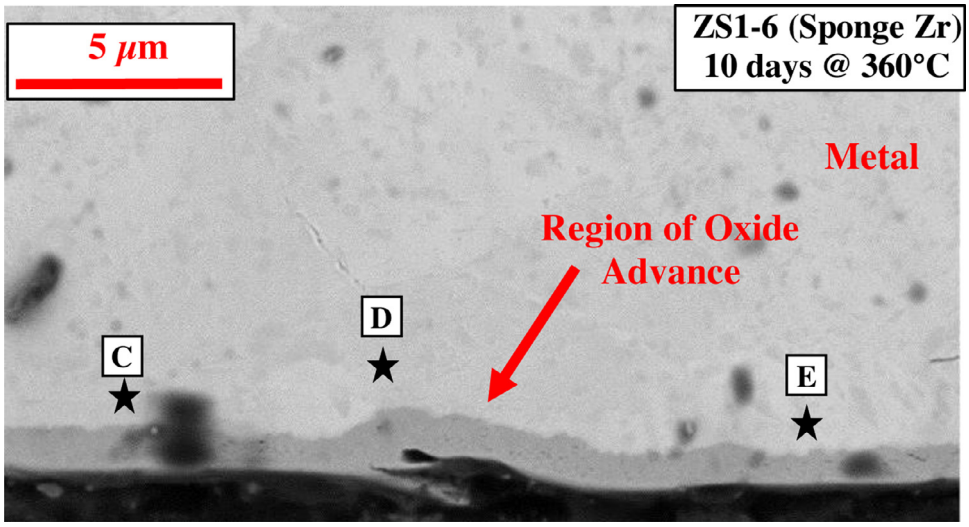

Fig. 9. SEM image of ZS1–6 after 10 days of exposure at 360 °C, showing the region of oxide advance where an XRF map acquired via synchrotron radiation was performed. Locations of detailed fluorescence acquisition are marked C, D, and E. Image was acquired after examination at the APS and was not refinished to preserve the surface layer of material leaving some artifacts visible.

The fluorescence results suggest that the alloying element content in locations A, D, and E (regions in the metal ahead of where the oxide penetrated *less)* is higher than in locations B and C (regions in the metal ahead of where the finger-like oxide penetrated *more*). This observation is consistent with a higher alloying element content of transition elements being associated with lower oxide growth. The difference in alloying element content from region to region could potentially cause the uneven growth observed.

Another µXRF map was acquired at the 2-ID-D beamline at the APS on sponge Zr, which had been corroded for 10 days. This sample did not break away but did exhibit regions of accelerated oxide growth (similar to the one shown in an SEM micrograph of this sample in Fig. 7(d)). A large fluorescence map was set up in the vicinity of a region showing accelerated growth. Fig. 9 shows an SEM micrograph of sample ZS1–6 corroded for 10 days, with a region where oxide advances in the metal, as indicated (this image was acquired after the µXRF experiments and was not re-prepared to maintain the surface as it was examined at the beamline).

Fig. 9 shows the locations of the detailed fluorescence acquisition (100-second dwell time) marked C, D, and E (A and B were not within the area of this micrograph). Fig. 10 shows an overlay of an SEM micrograph on an Fe fluorescence map of the same region (acquired at 6 second dwell times and with a 0.25 µm step size), also suggesting faster advancement of the oxide layer into regions where the Fe content is lower. The results of the acquisition are also shown in Fig. 10.

The Fe fluorescence map shown in Fig. 10 suggests an inverse correlation between alloying element content ahead of the advancing oxide front and the degree of advancement of this front relative to the overall oxide thickness. Fig. 10 shows that the oxide layer grew more slowly in regions where precipitates were presumably

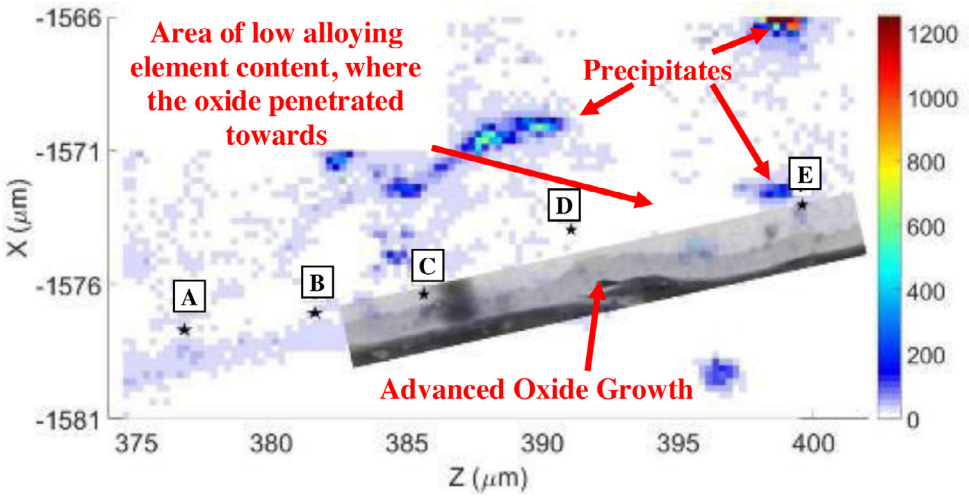

Fig. 10. (Top) Fe fluorescence overlaid with an SEM image of the sample (ZS1–6) examined with synchrotron XRF using the APS 2-ID-D beamline following 10 days exposure at 360 °C (same as that in Fig. 9); locations where long dwell fluorescence acquisitions were performed are labelled. (Bottom) Synchrotron XRF data acquired at 8.34 keV in five locations using the APS 2-ID-D beamline; for a given site, the Sn L, Cr Kα, and Fe Kα fluorescence counts are given normalized to the Zr L along with a description of the location; as can be seen, locations where the oxide did not penetrate have higher alloying element contents. The calculated error is based on standard deviation of the fluorescence counts before normalization and does not account for all forms of uncertainty.

located (regions of higher Fe fluorescence, visible near C and E) and penetrated faster in areas with the least amount of Fe (most amount of white). It is possible for this alloy, that the Fe was segregated due to final treatment in the low $\alpha+\beta$ region.

The heterogeneous distribution suggests a possible mechanism for instability formation during oxide growth in unalloyed Zr. While in an alloy such as Zircaloy-4 all grains have enough alloying element content to stabilize oxide growth, this may not be true in crystal bar or sponge Zr. Such variations could result from heterogeneous deformation or possibly from the presence of previous beta grains in one grain but not in the other. This may mean that in some grains there is not enough alloying element content to allow stable growth, causing a preferential advance of the oxide layer into that grain. This differential growth would cause stress with resulting mechanical breakup of the protective oxide layer. In contrast, for alloys with higher alloying element content, there is enough overall alloying content in every grain to produce stable growth.

4.4. Precursor oxide morphologies observed in samples prior to breakaway corrosion

The preliminary evidence from X-ray fluorescence suggests the possibility that the heterogeneous distribution of alloying elements leads to instabilities in oxide growth, whereby the oxide advances faster in regions with lower alloying element content. These regions of advanced oxide growth, shown in Figs. 6 and 7, appear prior to breakaway oxidation, suggesting that they are precursors to its occurrence. Fig. 11(A) shows SEM micrographs of the surface and underlying oxide of a sample (sponge Zr) corroded for 10 days. The right image in Fig. 11(A) was acquired by selectively milling away material using FIB to reveal a region of advanced oxide growth underneath the nodule-like formation observed on the surface of the oxide. This shows a correlation between the nodule-like oxide morphologies and preferential oxide advancement into the metal.

Two other possible precursor morphologies to breakaway growth were identified. These were grain boundary penetrations of the oxide and grain-to-grain differential growth of the oxide, as illustrated in Fig. 11. Fig. 11(B) shows an SEM micrograph of an oxide layer formed on ZC1–12 (crystal bar Zr) after a 10-day exposure. On the left is a plan-view image showing a complex topography of oxide grains, indicating that oxide growth occurs faster in some grains than others. The right image in Fig. 11(B) shows an SEM micrograph of a cross-section selectively milled using the FIB of the indicated location in the left image, showing significant preferential oxide growth along a grain boundary. The crystal bar sample shown in Fig. 11(B), was experiencing breakaway corrosion, but in the area where these images were taken, the surface of the sample was a cloudy gray (rather than white), suggesting breakaway had not yet fully occurred in this region, again illustrating the precursor character of these features.

Fig. 11(C) shows the results from an EBSD examination of a metal-oxide interface formed on sponge Zr after exposure for 10 days in regions in which local advanced oxide growth is overlaid with an SEM micrograph. The local advanced oxide growth (highlighted with red arrows) forms in regions corresponding to different metal grains, which are shown with different colors in Fig. 11(C). The colors represent different orientations of the hexagonal metal Zr grains. Fig. 11 (bottom) shows schematically the range of oxide morphologies that were found to be associated with unstable oxide growth. The most common oxide morphology associated with unstable growth in this study appears to be the small nodule-like features observed in every model Zr alloy and shown in Fig. 6, and not observed in Zircaloy-4. As the oxide layer grows, the nodule-like formations (which could form dependent on processing or alloying element distribution) may become larger and combine to form larger regions of spalling oxide. A hypothesis that could explain the observed behavior is that a heterogeneous distribution of alloying elements in the relatively pure Zr alloys leads to the preferential growth of oxide and associated nodule formation. The resulting stresses in the oxide could lead to oxide cracking and easy water access to the metal-oxide interface.

As discussed in Sections 4.1 and 4.2, the observed breakaway corrosion on the Zr-0.2Sn alloy with no signs of breakaway corrosion on the Zr-0.1Sn and Zr-0.4Sn alloy could suggest an alternative alloying element distribution effect leading to breakaway corrosion. It may be that around 0.2 wt.% Sn that there is threshold amount of Sn that increases the rate of Zr oxidation. This is evidenced by 40–50% higher weight gain in the Zr-0.4Sn alloy compared to the Zr-0.1Sn alloy. If the Zr-0.2Sn alloy was near this threshold, it may increase grain-to-grain differential corrosion and contribute to increased oxide stresses and lead to breakaway corrosion.

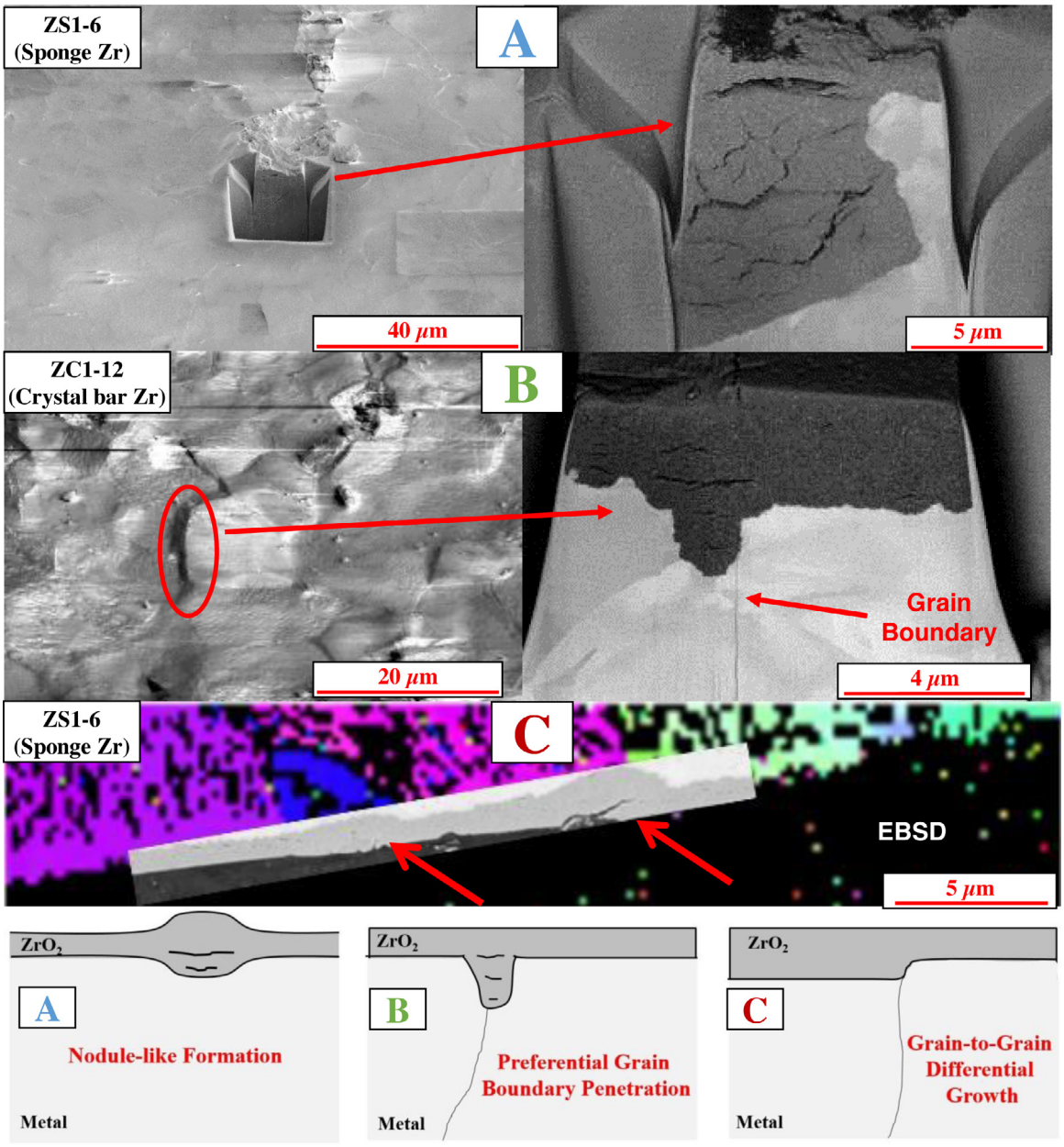

Fig. 11. (A) Nodule-like precursor morphology imaged with SEM formed on ZS1 (sponge Zr) after 10 days in autoclave at 360ºC. (B) Grain boundary penetration precursor morphology imaged with SEM formed on ZC1–12 (Crystal Bar Zr) after 10 days of exposure at 360 °C. (C) EBSD, overlaid with an SEM image, on ZS1–6 (sponge Zr) corroded in autoclave with 360 °C water for 10 days showing differential oxide growth along different metal grains. (Bottom) Schematic of three different precursor oxide morphologies to breakaway corrosion in Zr and Zr alloys with small amounts of alloying elements.

While the evidence presented in this paper suggests that (a) nodule-like features of advanced oxide form in pure Zr and Zr alloys with low alloying element content and (b) that these are linked to heterogeneous distribution of alloying elements (using synchrotron X-ray fluorescence), the limited amount of data (both sample exposures and XRF) prevents a final determination on the cause of the accelerated oxide growth in these alloys and this hypothesis should be tested further. A number of studies have been performed on grain-to-grain differential growth during corrosion in alloys with stable oxide growth layers, [31,32]. It is also possible that this affects the accelerated corrosion that is observed in-reactor. Thus, future work in this area could explore more specifically and thoroughly the precursor morphologies identified in this paper as potential causes of breakaway corrosion in pure Zr and Zr with small alloying element additions.

5. Conclusions

An investigation into the possible causes of breakaway corrosion and the effects of elements on the stabilization of oxide growth on zirconium and zirconium alloys was performed using a variety of techniques. Model Zr alloys were fabricated with low alloying element contents and corrosion tested in 360 °C water. After corrosion tests, the samples were examined to reveal oxide morphology and microchemistry. The conclusions are as follows:

1. During corrosion in autoclave with 360 °C water, breakaway oxidation (unstable oxide growth) was observed in two alloys (crystal bar Zr and Zr-0.2Sn) which was characterized by finger-like oxide penetrations into the metal. These penetrations advanced into regions of the crystal bar Zr metal with lower al-

loying element concentrations according to preliminary synchrotron microbeam X-ray fluorescence data.
2. The results suggest that a possible cause of unstable oxide growth is differential oxide growth in neighboring metal grains. This differential growth then generates stresses that cause oxide layer cracking and allow easy ingress of water to the underlying metal. This differential growth can occur between grains, along grain boundaries, or, in general, in regions where the alloying element content varies. Other possible root causes for breakaway corrosion in pure Zr and Zr alloys with low alloying elements should continue to be explored, as the experiments in this study are only preliminary.
3. Possible precursors of this unstable growth were also observed on the oxide surface. After testing in autoclave with 360 °C water, nodule-like oxide formations were observed in the model alloys (but not on Zircaloy-4). Beneath these nodules regions of advanced oxide growth were observed. These nodules were seen only in low alloying element alloys such as the pure Zr and model Zr alloys (with Sn, Fe, and Cr) created for this study, but not in Zircaloy-4.

The preliminary investigations into the corrosion resistance of the model alloys fabricated in this study has pointed to a number of possible causes of breakaway corrosion linked to alloying element distribution. Future studies with advanced chemical characterization techniques, such as atom probe tomography (APT) or time-of-flight secondary ion mass spectrometry (TOF-SIMS) examining similar materials with low levels of alloying elements may better characterize the role specific alloying elements (for instance the cause of the instabilities in the Zr-0.2Sn alloy) play in causing unstable oxide growth and should be pursued.

Declaration of Competing Interest

The authors declare that they have no known competing financial interests or personal relationships that could have appeared to influence the work reported in this paper.

CRediT authorship contribution statement

B. Ensor: Conceptualization, Formal analysis, Investigation, Visualization, Writing – original draft. **A.T. Motta:** Conceptualization, Writing – review & editing, Supervision. **A. Lucente:** Conceptualization, Writing – review & editing, Supervision. **J.R. Seidensticker:** Conceptualization, Supervision. **J. Partezana:** Resources. **Z. Cai:** Methodology, Resources.

Acknowledgements

The authors would like to thank Jessica Gee for her help in this work in the context of her undergraduate honors thesis in nuclear engineering at Penn State. Additionally, we thank Ross Luther for his help in fabricating the samples. This research has been authored by Fluor Marine Propulsion, LLC under Contract No. DOE-89233018CNR000004 with the U.S. Department of Energy. This research used resources of the Advanced Photon Source, a U.S. Department of Energy (DOE) Office of Science User Facility operated for the DOE Office of Science by Argonne National Laboratory under Contract No. DE-AC02–06CH11357. This research was performed (B. Ensor) under appointment to the Rickover Fellowship Program in Nuclear Engineering sponsored by Naval Reactors Division of the U.S. Department of Energy.

References

[1] S. Kass, "The Development of the Zircaloys", Symposium on Corrosion of Zirconium Alloys ASTM STP 368, pp. 3-27, 1964.
[2] B. Cox, "Some thoughts on the mechanisms of in-reactor corrosion of zirconium alloys", J. Nucl. Mater. 336 (2005) 331–368.
[3] T. Ahmed, L.H. Keys, "The breakaway oxidation of zirconium and its alloys a review", J. Less-Common Metals 39 (1975) 99–107.
[4] C. Lemaignan, A.T. Motta, "Zirconium Alloys in Nuclear Applications", Mater. Sci. Technol. A Comprehensive Treatment (1994) 1–51.
[5] T.R. Allen, R.J.M. Konings, A.T. Motta, "Corrosion of Zirconium Alloys", in Comprehensive Nuclear Materials, vol. 5, R. J. M. Konings, Ed., Oxford, UK, Elsevier, 2012, pp. 49-68.
[6] A.T. Motta, A. Couet, R.J. Comstock, "Corrosion of zirconium alloys for nuclear fuel cladding", Annu. Rev. Mater. Res. 45 (2015) 311–343.
[7] E. Hillner, "Corrosion of Zirconium-Base Alloys- An Overview", Zirconium in the Nuclear Industry, ASTM STP 633, pp. 211-235, 1977.
[8] A.T. Motta, M.J.G. da Silva, A. Yilmazbayhan, R.J. Comstock, Z. Cai, B. Lai, "Microstructural characterization of oxides formed on model Zr alloys using synchrotron radiation", J. ASTM Int. 5 (3) (2008) JAI101257 1-20.
[9] J.N. Wanklyn, P.J. Jones, "The aqueous corrosion of reactor metals", J. Nucl. Mater. 6 (3) (1962) 291–329.
[10] D.H. Bradhurst, P.M. Heuer, "The influence of oxide stress on the breakaway oxidation of Zircaloy-2", J. Nucl. Mater. 37 (1970) 35–47.
[11] R.A. Ploc, "Breakaway oxidation of Zirconium at 573 K", J. Nucl. Mater. 82 (1979) 411–418.
[12] M. Steinbrueck, F.O. da Silva, M. Grosse, "Oxidation of Zircaloy-4 in steam-nitrogen mixtures at 600-1200°C", J. Nucl. Mater. 490 (2017) 226–237.
[13] B. de Gabory, Y. Dong, A.T. Motta, E.A. Marquis, "EELS and atom probe tomography study of the evolution of the metal/oxide interface during zirconium alloy oxidation", J. Nucl. Mater. 462 (2015) 304–309.
[14] N. Ni, D. Hudson, J. Wei, P. Wang, S. Lozano-Perez, G.D.W. Smith, J.M. Sykes, S.S. Yardley, K.L. Moore, S. Lyon, R. Cottis, M. Preuss, C.R.M. Grovenor, "How the crystallography and nanoscale chemistry of the metal/oxide interface develops during the aqueous oxidation of zirconium cladding alloys", Acta Mater 60 (20) (2012) 7132–7149.
[15] Y. Dong, A.T. Motta, E.A. Marquis, "Atom probe tomography study of alloying element distributions in Zr alloys and their oxides", J. Nucl. Mater. 442 (2013) 270–281.
[16] J. Hu, T. Aarholt, B. Setiadinata, K. Li, A. Garner, S. Lozano-Perez, M. Moody, P. Frankel, M. Preuss, C. Grovenor, "A multi-technique study of "barrier layer" nano-porosity in Zr oxides during corrosion and hydrogen pickup using (S)TEM, TKD, APT and NanoSIMS", Corros. Sci. 158 (2019).
[17] J.N. Wanklyn, C.F. Britton, D.R. Silvester, N.J.M. Wilkins, "Influence of environment on the corrosion of zirconium and its alloys in high-temperature steam", J. Electrochem. Soc. 110 (8) (1963) 856–866.
[18] R.A. Ploc, "An electron microscope study of breakaway oxidation of zirconium at 623 K", J. Nucl. Mater. 91 (1980) 322–328.
[19] Y. Yan, T.A. Burtseva, M.C. Billone, "High-temperature steam-oxidation behavior of Zr-1Nb cladding alloy E110", J. Nucl. Mater. 393 (2009) 433–448.
[20] H.-.G. Kim, I.-.H. Kim, B.-.K. Choi, J.-.Y. Park, "A study of the breakaway oxidation behavior of zirconium cladding materials", J. Nucl. Mater. 418 (2011) 186–197.
[21] M. Grosse, M. Steinbrueck, B. Schillinger, A. Kaestner, "In Situ investigations of the hydrogen uptake of zirconium alloys during steam oxidation", Zirconium Nucl. Ind.: 18th Int. Sympos. 1597 (2018) 1114–1135 STP.
[22] D. Arias, J.P. Abriata, "The Fe-Zr (Iron-Zirconium) System", Bull. Alloy Phase Diagram. 9 (5) (1988) 597–604.
[23] H. Okamoto, "Sn-Zr (Tin-Zirconium)", J. Phase Equilibria Diffus. 31 (2010) 411–412.
[24] H. Okamoto, "Supplemental literature review of binary phase diagrams: b-Fe, Cr-Zr, Fe-Np, Fe-W, Fe-Zn, Ge-Ni, La-Sn, La-Ti, La-Zr, Li-Sn, Mn-S, and Nb-*Re*", J. Phase Equilibria Diffusion 37 (2016) 621–634.
[25] ASTM"Standard G2/G2M - 06", ASTM International, West Conshohocken, PA, 2011.
[26] D.J. Spengler, A.T. Motta, R. Bajaj, J.R. Seidensticker, Z. Cai, "Characterization of Zircaloy-4 corrosion films using microbream synchrotron radiation", J. Nucl. Mater. 464 (2015) 107–118.
[27] J. Gee, "An Investigation of the Effect of Tin on Zirconium Alloy Oxide Morphology", Honors Thesis in Nuclear Engineering: The Pennsylvania State University, 2015.
[28] A. Yilmazbayhan, O. Delaire, A.T. Motta, R.C. Birtcher, J.M. Maser, B. Lai, "Determination of the alloying content in the matrix of Zr alloys using synchrotron radiation microprobe X-ray fluorescence", J. Nucl. Mater. 321 (2003) 221–232.
[29] A. Couet, A.T. Motta, B. de Gabory, Z. Cai, "Microbeam X-ray Absorption Near-Edge Spectroscopy study of the oxidation of Fe and Nb in zirconium alloy oxide layers", J. Nucl. Mater. 452 (2014) 614–627.
[30] A. Couet, A. Motta, A. Ambard, "The coupled charge compensation model for zirconium alloy fuel cladding oxidation, I. Parabolic oxidation of zirconium alloys", Corros Sci 100 (2015) 73–84.
[31] A. Garner, P. Frankel, J. Partezana, M. Preuss, "The effect of substrate texture and oxidation temperature on oxide texture development in zirconium alloys", J. Nucl. Mater. 484 (2017) 347–356.
[32] J.A. Szpunar, W. Qin, H. Li, N.A.P.K. Kumar, "Roles of texture in controlling oxidation, hydrogen ingress and hydride formation in Zr alloys", J. Nucl. Mater. 427 (2012) 343–349.
[33] E. Hillner, D.G. Franklin, J.D. Smee, "Long-term corrosion of Zircaloy before and after irradiation", J. Nucl. Mater. 278 (2000) 334–345.